Hydrogen from Biogas: Dynamic Modeling of an Integrated Shift Reactor

Edwin Hirtreiter*, Andy Gradel, Hans-Peter Schmid, Christopher Wünning, Sebastian Rehfeldt and Harald Klein

DOI: 10.1002/cite.12007

This is an open access article under the terms of the Creative Commons Attribution License, which permits use, distribution and reproduction in any medium, provided the original work is properly cited.



Supporting Information available online

A dynamic, pseudo-homogeneous, two-dimensional reactor model of an integrated shift reactor for the production of hydrogen from biogas is developed. This integrated shift reactor enables the preheating of the biogas feed through a helical coil in the fixed bed. Simultaneously, the resulting reduced temperatures in the fixed bed lead to an increased hydrogen yield of the shift reactor, due to the exothermicity of the water-gas shift reaction. The developed model is validated with steady-state and dynamic operating data from a measurement campaign at a pilot biogas steam reforming plant. The results show that the model adequately predicts the measured operating points.

Keywords: Biogas, Dynamic simulation, Hydrogen, Reactor model, Water-gas shift

Received: March 07, 2025; revised: April 28, 2025; accepted: May 08, 2025

1 Introduction

Biogas is produced through the anaerobic digestion of organic materials, such as animal manure or energy crops. It primarily consists of 45–70 vol.-% methane and 25–55 vol.-% carbon dioxide, with trace amounts of sulfur compounds, ammonia, nitrogen, oxygen, and siloxanes [1–3]. The actual composition largely depends on the feedstock and the operating conditions of the fermenter [1, 2].

In 2022, almost 9900 biogas plants were in operation in Germany [4]. These biogas plants covered around 6 % of Germany's electricity demand in 2023 [5]. Thus, biogas contributes significantly to our renewable energy system. The feed-in tariffs for electricity from these biogas plants are typically subsidized by the Renewable Energy Sources Act (EEG). However, those subsidies expire after 20 years of operations, and plans for a continued operation need to be made [6–9]. Options include, e.g., application for continued remuneration in the EEG, flexible electricity production, switching to biomethane, or the production of hydrogen from biogas. The latter could promote the national rampup of the hydrogen industry and the development of local hydrogen hubs.

The steam reforming process, which is the state-of-theart process for the production of hydrogen from natural gas [10, 11], can be leveraged to produce green hydrogen from biogas. Therefore, the technology readiness level (TRL) of biogas reforming is estimated to 7–8 [12]. Firstly, biogas is cleaned in active carbon beds, compressed and fed to a hydrodesulfurization (HDS) reactor. Subsequently, the cleaned biogas is converted with steam into syngas in a steam reformer. A shift reactor then increases the hydrogen content in the syngas, followed by a pressure swing adsorption (PSA) that purifies the gas stream to produce fuel cell-grade hydrogen. The tail gas of the PSA is fired together with biogas in the steam reformer furnace. The

¹Edwin Hirtreiter https://orcid.org/0000-0002-0693-925X (edwin.hirtreiter@tum.de), ²Dr.-Ing. Andy Gradel,

³Dr.-Ing. Hans-Peter Schmid, ⁴Christopher Wünning,

https://orcid.org/0000-0002-3650-9533,

Check for updates

¹Dr.-Ing. Sebastian Rehfeldt

¹Prof. Dr.-Ing. Harald Klein

¹Technical University of Munich, TUM School of Engineering and Design, Department of Energy and Process Engineering, Institute of Plant and Process Technology, Boltzmannstraße 15, 85748 Garching, Germany.

²BtX energy GmbH, Esbachgraben 1, 95463 Bindlach, Germany.

³WS Reformer GmbH, Dornierstraße 14, 71272 Renningen, Germany.

⁴RWTH Aachen, Lehrstuhl für Nachhaltige Thermoprozesstechnik und Institut für Industrieofenbau und Wärmetechnik, Kopernikusstraße 10, 52074 Aachen, Germany.

ded from https://onlinelibrary.wiley.com/doi/10.1002/cite.12007 by Rwth Aachen University

eingang, Wiley Online Library on [12/06/2025]. See the Terms and Conditions (https://onlinelil

conditions) on Wiley Online Library for rules of use; OA articles are governed by the applicable Creative Commons Licensu

Figure 1. Biogas steam reforming plant of the company BtX energy GmbH, installed in Krefeld.

process described has recently completed its pilot phase operation. Fig. 1 shows the steam reforming plant of the project BioH2Ref installed at a biogas plant in Krefeld.

Besides the steam reformer, the shift reactor is a core equipment to increase the hydrogen yield. A shift reactor is typically an adiabatic fixed-bed reactor with an insulated pressure shell filled with catalyst. Syngas from the reformer is fed to the reactor, and the equilibrium-limited water-gas shift (WGS) reaction proceeds, as denoted in Eq. (1). Due to the exothermicity, indicated by a negative molar reaction enthalpy $\Delta \tilde{H}_R$ of the reaction, heat is produced inside the reactor, causing an adiabatic temperature rise. Therefore, the reaction equilibrium is favored towards hydrogen at low

temperatures.

$$CO + H_2O \rightleftharpoons CO_2 + H_2 \quad \Delta \bar{H}_R < 0 \tag{1}$$

For shift reactors, a distinction is usually made between two temperature regimes: High-temperature (HT) shift reactors operate at temperatures of 350–450 °C [13, 14]. Commonly, ferrochrome catalysts are used [13, 14]. In contrast, low-temperature (LT) shift reactors exhibit temperatures of 190–250 °C and copper-zinc-aluminum catalysts are employed [13, 14]. In large-scale hydrogen plants, the syngas is typically first fed into an HT shift, then cooled to around 200 °C and fed into an LT shift, as generically depicted in

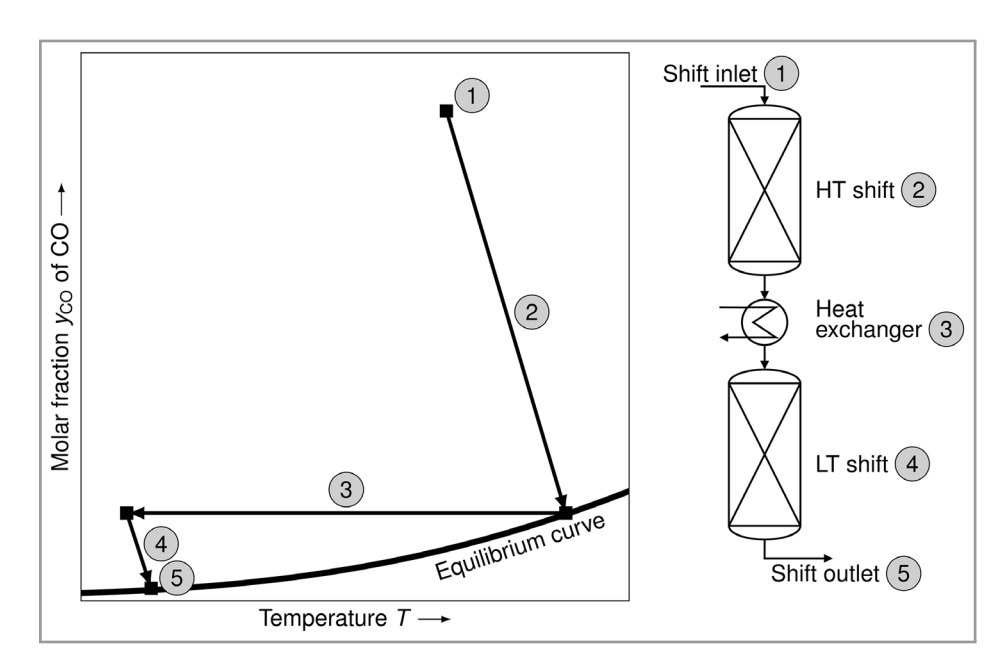


Figure 2. Shift reactor configuration of large-scale hydrogen plants.

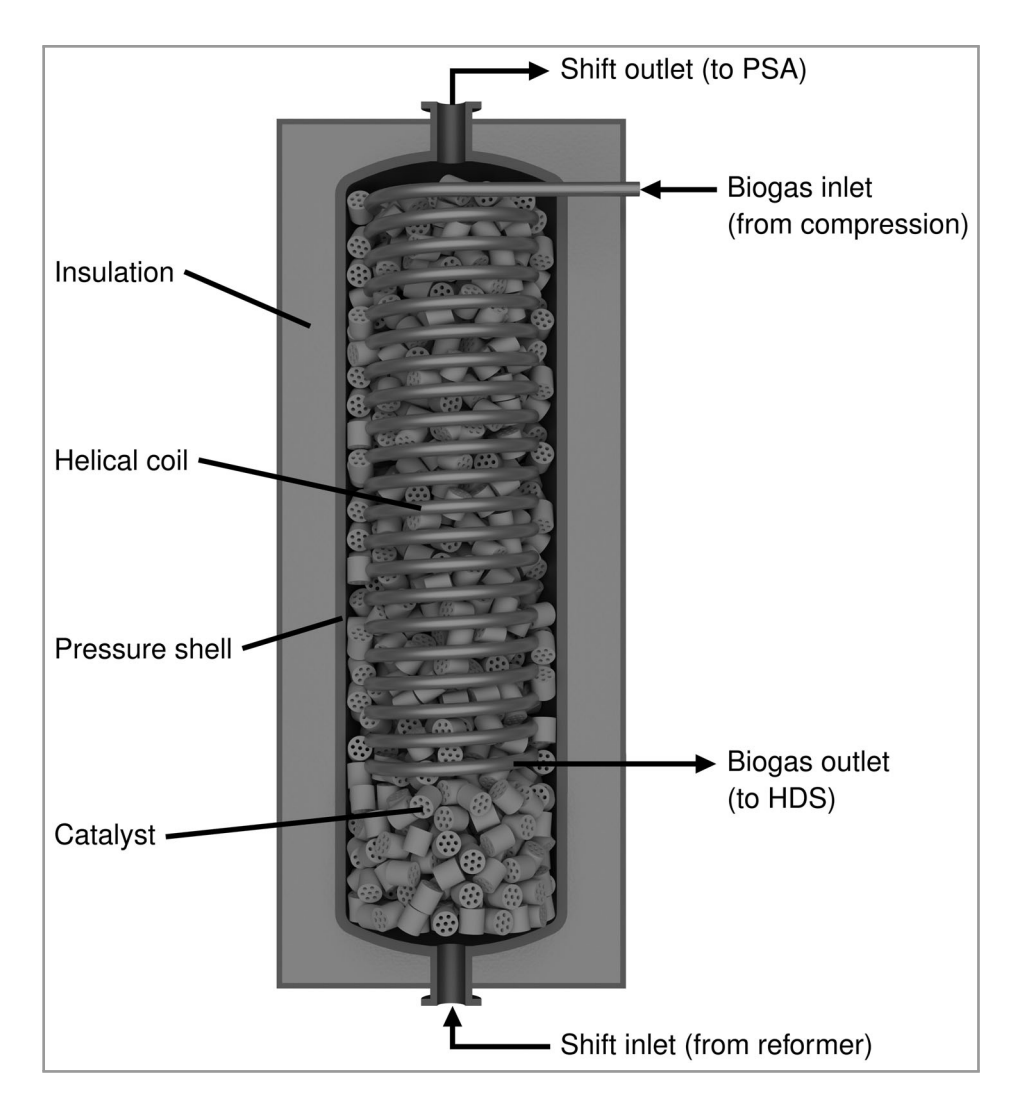


Figure 3. Schematic illustration of the integrated shift reactor from the company WS Reformer GmbH.

ingang, Wiley Online Library on [12/06/2025]. See the Terms

-conditions) on Wiley Online Library for rules of use; OA articles are governed by the applicable Creative Commons

Fig. 2. This approach leverages faster reaction kinetics at high temperatures and thus enables high carbon monoxide (CO) conversion rates in the HT shift. The LT shift can further reduce CO molar fractions due to a favorable reaction equilibrium at lower temperatures.

A highly integrated and compact design of major equipment was required to build a small-scale, containerized biogas steam reforming plant. Therefore, the heat produced due to the exothermic WGS reaction is used in our integrated shift reactor, and a helical coil is installed in the fixed bed for this purpose, as depicted in Fig. 3. This helical coil is used to preheat the biogas feed for the HDS reactor in a countercurrent stream configuration. The CO outlet fraction is reduced as a side effect of the cooling. The bottom part of the shift reactor remains adiabatic to start the WGS reaction.

Various reactor models of shift reactors have been developed for large-scale processes, such as integrated gasification combined-cycle power plants [15, 16] or ammonia plants [17], as well as for small-scale processes, e.g., for fuel

cell applications [18–21] or laboratory setups [22–24]. These models were developed with varying levels of detail. In pseudo-homogeneous models [20, 22, 24, 25], it is assumed that the gas temperature is equal to the temperature of the solid catalyst phase. In contrast, in heterogeneous reactor models [15, 16, 18, 19, 21, 26], the gas phase is treated separately from the solid catalyst phase. Therefore, the catalyst temperature may exhibit a different temperature than the gas phase. Furthermore, the developed shift reactor models can be divided into one-dimensional (1D) [15, 16, 19, 21, 22, 24, 26] and two-dimensional (2D) [18, 20, 25] models. In addition, a distinction can be made between steady-state [15, 19–21, 25] and dynamic models [16, 18, 26].

Besides reactor models for HT [16, 22, 24] and LT shift [16, 19, 21], models with integrated heat exchangers are developed. Paixão et al. [25] developed a steady-state, pseudo-homogeneous, 2D reactor model for a multitubular shift reactor. The WGS reaction proceeds on the tube side, and the generated heat is dissipated by boiling water on the shell side of the reactor tubes. The model is used to

15222640, 0, Downloaded from https://onlinelibrary.wiley.com/doi/10.1002/cite.12007 by Rwth Aachen University

Zentraler Rechnungseingang, Wiley Online Library on [12/06/2025]. See the Terms

nditions) on Wiley Online Library for rules of use; OA articles are governed by the applicable Creative Commons License

Research Article

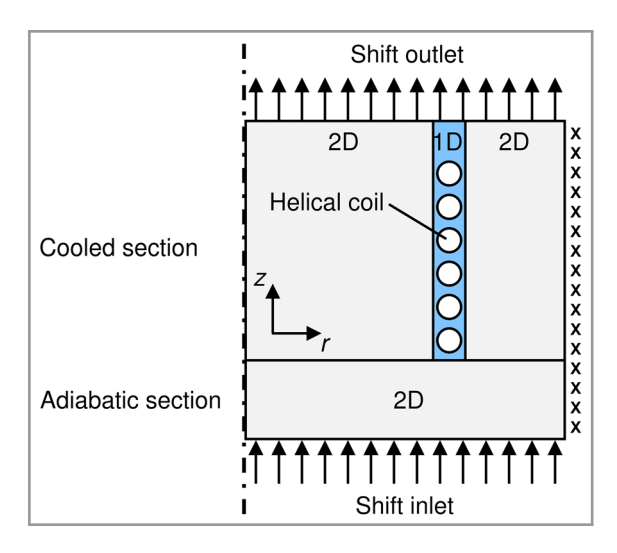


Figure 4. Segmentation of the shift reactor with the axial domain z and the radial domain r for modeling.

optimize the reactor based on a cost function considering both capital and operational expenses. Similarly, Rosner et al. [27] consider an isothermal WGS reactor and introduce a dimensionless rate optimization number to optimize reaction temperatures. Saw and Nandong [26] propose a reactor configuration with a reactor divided into two reaction zones and an interstage cooling zone in between. A 1D, heterogeneous reactor model is utilized to investigate the effects of the position of the interstage cooling zone and different control strategies.

In this paper, an approach for dynamic modeling of an integrated shift reactor with a pseudo-homogeneous, 2D reactor model is proposed. The novelty of our integrated shift reactor is that the syngas is derived from biogas, and the fluid inside the helical coil is not boiling water but the biogas feed itself being preheated for the HDS reactor. To validate the developed model, dynamic step tests are performed at the pilot plant in Krefeld, and the measurements are compared to the model results.

2 Model Development

The developed shift reactor model is a dynamic, pseudo-homogeneous, 2D model. Because of the presence of the helical coil, the model is divided into multiple subsystems, as illustrated in Fig. 4. The bottom part of the reactor is modeled as a 2D, adiabatic reactor segment. The upper part of the reactor is divided into three zones: a 2D cylindrical reactor core, a 1D cooling zone containing the helical cooling coil, and a surrounding 2D cylindrical ring element. As the pressure shell of the reactor is insulated, no heat losses to the atmosphere are assumed. The only radial phenomenon considered in the 2D reactor segments is heat conduction. Axial heat conduction as well as radial and axial diffusion are neglected.

Since pressure effects are on significantly faster time scales than temperature effects, the momentum balance is reduced to a quasi-steady-state 1D pressure drop relation, namely the Ergun equation [28] according to [29]. The pressure drop is calculated based on the inlet gas properties and velocity.

2.1 Two-Dimensional Reactor Segments

The component mass balance on a finite volume gives

$$\varepsilon \frac{\partial (w_i \rho)}{\partial t} = -\frac{\partial (v w_i \rho)}{\partial z} + \rho_{\text{cat}} v_i r_{\text{reac}} \bar{M}_i$$

$$\forall i \in [\text{CO, CO}_2, \text{ H}_2\text{O, H}_2, \text{ CH}_4].$$
(2)

The accumulation term is determined with the mass fraction w_i of component i, the gas density ρ , the time t, and the porosity $\varepsilon=0.5$ [16]. On the right side, the convective mass transport is described with the superficial velocity ν along the axis z of the reactor. The consumption and formation of components is calculated from the reaction kinetics in Sect. 2.3 with the molar reaction rate $r_{\rm reac}$, which is related to the catalyst mass. The molar mass of component i is denoted with \bar{M}_i . The bulk density $\rho_{\rm cat}$ of the catalyst is 1100 kg m⁻³. The stochiometric number ν_i is, corresponding to Eq. (1), negative for educts and positive for products ($\nu_{\rm CO} = \nu_{\rm H_2O} = -1$, $\nu_{\rm CO_2} = \nu_{\rm H_2} = +1$).

The energy balance of a 2D reactor segment can be derived as

$$\frac{\partial \tilde{u}}{\partial t} = -\frac{\partial (\rho \, v \, h)}{\partial z} + \frac{1}{r} \, \frac{\partial}{\partial r} \left(F_{\lambda} \, \lambda_{e} \, r \, \frac{\partial T}{\partial r} \right). \tag{3}$$

The right side of the energy balance consists of a convective term and a term to describe the heat conduction along the radial domain r. The radial effective heat conductivity λ_e comprises a static contribution, according to Zehner and Schlünder [30], and a dynamic contribution, according to Specchia et al. [31]. Therefore, the catalyst heat conductivity is assumed to be 0.1 W m⁻¹K⁻¹ [16]. A constant fitting parameter F_{λ} is introduced to adjust the radial effective heat conductivity according to experimental data.

The volume-specific internal energy \tilde{u} , defined as

$$\tilde{u} = \rho_{\text{cat}} c_{\text{cat}} (T - 298.15 \text{ K}) + \varepsilon \left(\rho h - p\right), \tag{4}$$

comprises the specific heat capacity $c_{\text{cat}} = 920 \text{ J kg}^{-1}\text{K}^{-1}$ of the catalyst, the temperature T, the specific gas enthalpy h, and the pressure p.

2.2 One-Dimensional Reactor Segment

The 1D segment comprises two subsystems: the fixed bed and the helical cooling coil. These subsystems are coupled by heat transfer.

The component mass balance is identical to the 2D component balance in Eq. (2) but only a function of the axial domain, whereas the energy balance of the 1D segment in

Eq. (5) is modified to comprise the heat transfer to the helical coil and the heat conduction to the surrounding 2D segments.

$$\frac{\partial \tilde{u}}{\partial t} = -\frac{\partial (\rho v h)}{\partial z} - \dot{q} \frac{A_{w}}{L A_{1D}} - \lambda_{e}|_{r=R_{i}} \frac{2\pi R_{i}}{A_{1D}} \frac{\partial T}{\partial r}|_{r=R_{i}} + \lambda_{e}|_{r=R_{o}} \frac{2\pi R_{o}}{A_{1D}} \frac{\partial T}{\partial r}|_{r=R_{i}}$$
(5)

The heat transfer to the coil is calculated by the heat flux \dot{q} and the volume-specific heat exchange area of the coil in relation to the volume of the 1D segment. Here, the heat exchange area $A_{\rm w}$ of the helical coil, the length L of the reactor segment, and the cross-section $A_{\rm 1D}$ of the 1D segment are required. The heat conduction from the reactor core or the outer cylindrical ring to the 1D segment is determined by calculating the temperature gradient, the volume-specific lateral surface area of the cylindrical 1D segment, and the effective bed conductivity at the inner radius $R_{\rm i}$ and the outer radius $R_{\rm o}$ of the 1D segment. Due to confidentiality reasons, the dimensions of the reactor and the helical coil cannot be declared.

The heat transferred to the helical coil depends on the current temperature T at position z in the fixed-bed and the corresponding temperature $T_{\rm b}$ of the biogas stream in the helical coil. Using the calculated overall heat transfer coefficient k and the equation

$$\dot{q} = F_{\rm k} k (T - T_{\rm b}), \tag{6}$$

the area-specific heat flow \dot{q} can be calculated and adjusted to experimental data by a constant factor F_k . This heat flow is uniformly distributed through the narrow 1D segment, whose diameter is approximately the diameter of the helical coil. The heat transfer coefficients are calculated using Gnielinski correlations [32, 33] according to [29], assuming transverse flow conditions for the fixed-bed side of the helical coil and pipe flow in a helical coil on the inside.

Analogously to the reactor segments, the momentum balance of the helical coil is reduced to the quasi-steady-state 1D pressure drop relation of Gnielinski [33] according to [29]. Therefore, the mass balance of the biogas stream inside the helical coil,

$$0 = -\frac{\partial \dot{M}_{b}}{\partial z'},\tag{7}$$

is assumed to be also quasi-steady state. Here, $\dot{M}_{\rm b}$ denotes the mass flow rate of the biogas inside the helical coil. The axial discretization z' is the same as for the reaction side, but the direction is flipped. The reason for this is explained in Sect. 2.4.

The energy balance of the cooling coil is given with the enthalpy $h_{\rm b}$ of the biogas stream, the length $L_{\rm c}$ of the coil, and the cross-section of the coil $A_{\rm c}$ by

$$\frac{L_{c}}{L} \frac{\partial \tilde{u}_{b}}{\partial t} = -\frac{1}{A_{c}} \frac{\partial \left(\dot{M}_{b} h_{b}\right)}{\partial z'} + \dot{q} \frac{A_{w}}{L A_{c}}.$$
 (8)

Here, the volume-specific internal energy \tilde{u}_b of the gas stream inside the helical coil is defined by the pressure p_b , and the density ρ_b of the biogas as

$$\tilde{u}_{b} = \rho_{b} h_{b} - p_{b}. \tag{9}$$

15222640, 0, Downloaded from https://onlinelibrary.wiley.com/doi/10.1002/cite.12007 by Rwth Aachen University

Rechnungseingang, Wiley Online Library on [12/06/2025]. See the Terms and Conditions (https://onlinelibrary.wiley.com/term

and-conditions) on Wiley Online Library for rules of use; OA articles are governed by the applicable Creative Commons License

2.3 Kinetics

The implemented reaction kinetics is a power law model according to Hla et al. [34], as denoted in Eq. (10). They determined the parameters of this power law model, based on partial pressures p_i , using a commercially available ferrochrome catalyst. The activation energy $E_{\rm A}$ is 88 kJ mol⁻¹ and \bar{R} denotes the molar universal gas constant.

$$r_{\text{reac}} = F_{\text{p}} \ 10^{0.659} \ \exp\left(\frac{-E_{\text{A}}}{\bar{R}T}\right) \ p_{\text{CO}}^{0.9} \ p_{\text{H}_2\text{O}}^{0.31} \ p_{\text{CO}_2}^{-0.156} \ p_{\text{H}_2}^{-0.05}$$

$$\times \left(1 - \frac{1}{K} \ \frac{p_{\text{CO}_2} \ p_{\text{H}_2}}{p_{\text{CO}} \ p_{\text{H}_2\text{O}}}\right)$$

$$(10)$$

The temperature-dependent equilibrium constant K is determined according to Twigg [35] by

$$K = \exp(Z(Z(0.63508 - 0.29353 Z) + 4.1778) + 0.31688)$$
(11)

with

$$Z = \frac{1000}{\left\lceil \frac{T}{K} \right\rceil} - 1. \tag{12}$$

Since the reaction kinetics was determined close to ambient pressures, using this kinetics directly at industrial pressures of a WGS reactor (e.g., 10–30 bar) would result in an overestimation of the reaction rates. Therefore, a pressure scale-up factor

$$F_{\rm p} = \frac{p_0^{0.5 - \frac{p_0}{250}}}{p_0^{1.004}} \tag{13}$$

is calculated from the inlet pressure p_0 and applied to the reaction rate in Eq. (10) [16, 36, 37].

2.4 Solution Procedure

The full equations system, as declared in Sect. S1 of the Supporting Information, is solved using Siemens gPROMS with its DAEBDF solver. The Peng-Robinson fluid package provides thermodynamic property data.

Axial discretization is performed using backward finite differences. This is the reason why the domain of the helical coil subsystem is flipped. This flipping allows the use of the backward finite difference scheme for both the helical coil and the reactor segments. Here, 10 axial discretization points are used for the adiabatic part and 25 for every segment in the cooled section. Radial discretization is handled

com/doi/10.1002/cite.12007 by Rwth Aachen University

eingang, Wiley Online Library on [12/06/2025]. See the Terms and Conditions (https://onlinelibrary.wiley.com/term

and-conditions) on Wiley Online Library for rules of use; OA articles are governed by the applicable Creative Commons Licensu

Figure 5. Working principle of the integrated shift reactor. Assumed inlet gas composition: $y_{H_2O} =$ 49.5 %, $y_{CO} = 5.8$ %, $y_{CH4} = 1.1$ %, $y_{\rm H_2} = 31.5 \%$, $y_{\rm CO_2} = 12.1 \%$.

per 2D segment).

Data Acquisition for Validation

To validate the shift reactor model, a measurement campaign was performed at the pilot plant in Krefeld. This pilot plant is a commercial-scale biogas reforming plant producing fuel cell-grade hydrogen from biogas. The biogas for this pilot plant is produced through anaerobic digestion at an actual biogas plant, which uses cow manure as feedstock.

As a pilot plant is not a laboratory system, parameters of the shift reactor cannot be set individually and independently of other plant parts. Therefore, the plant was operated at various operating points during the measurement campaign, and measurement data was logged around the shift reactor. Within the operating limits of the reforming plant, the reformer tube temperature, the reformer pressure, the steam-to-carbon ratio (S/C), and the load were varied with dynamic step tests. Temperatures in the fixed bed of the shift reactor were measured using type K thermocouples. The dry gas composition of the inlet and outlet stream of the shift were logged using EHEIM gas analyzers. Details about the acquisition of measurement data can be found in Sect. \$2 in the Supporting Information.

Results

4.1 Working Principle

Using the gPROMS model validation feature, the constant adjustment factors F_{λ} and F_{k} were fitted to a full-load operating point. The best fit was obtained with $F_{\lambda}=1.68$ and $F_{\rm k} = 0.83$.

To illustrate the working principle of the integrated shift reactor, Fig. 5 depicts the dry molar fraction y_{CO} of CO over the temperature T. The equilibrium curve, derived from Eq. (11) for a specific inlet gas composition, indicates that elevated temperatures result in increased molar fractions of CO due to the exothermicity of the WGS reaction. In purely adiabatic shift reactors, the molar fraction of CO decreases along the adiabatic curves, which are depicted as grey dashed lines in Fig. 5. These adiabatic curves are dependent on the reactor inlet temperature T_0 and the inlet gas composition. An adiabatic shift reactor can reduce the molar fraction of CO at most until the adiabatic curve intersects with the equilibrium curve. A further reduction of CO is only possible by decreasing the temperature of the reacting mixture, as depicted in Fig. 2 for a large-scale shift reactor

In the context of our integrated shift reactor, gas from the reformer is fed to the reactor at 341 °C with a dry molar fraction of CO of 11.6 %. As illustrated in Fig. 5, the bottom part of the integrated shift reactor is adiabatic. Consequently, the dry molar fraction of CO decreases initially along the adiabatic curves until reaction equilibrium is achieved. By cooling the catalyst bed in the upper part of the reactor through the helical coil, the dry molar fraction of CO can be further reduced alongside the equilibrium curve. However, due to slower reaction kinetics at reduced temperatures, the dry molar fraction of CO at the shift reactor outlet remains slightly above the equilibrium curve. In the illustrated case, the dry molar fraction of CO of the integrated shift reactor is reduced to 1.3 %. In comparison, a purely adiabatic shift reactor yields a dry molar fraction of CO of 2.1 % at the reactor outlet. In parallel, the biogas feed is preheated from 30 to 353 °C, ready for the HDS reactor.

Due to the positioning of the helical coil in a particular area of the fixed-bed, a 2D temperature profile is assumed

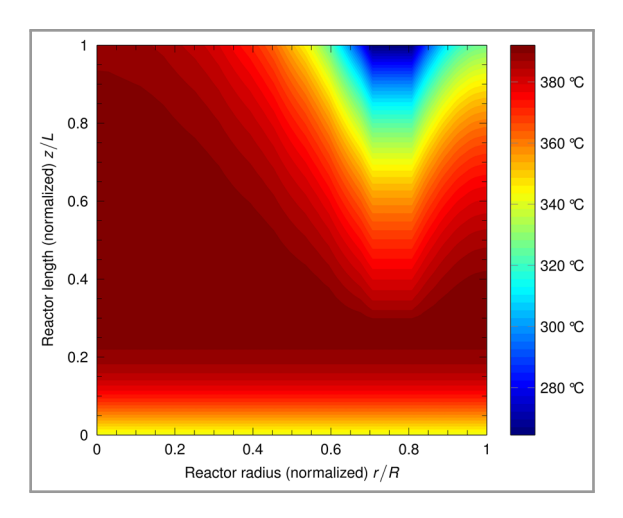


Figure 6. Simulated 2D temperature distribution of the integrated shift reactor. Assumed inlet gas composition: $y_{H_2O} = 49.5 \%$, $y_{CO} = 5.8 \%$, $y_{CH4} = 1.1 \%$, $y_{H_2} = 31.5 \%$, $y_{CO_2} = 12.1 \%$.

in the fixed bed, which can be confirmed through the developed model described in Sect. 2. For an exemplary case, the 2D temperature distribution is shown in Fig. 6. In the

adiabatic bottom of the reactor, the temperature isolines are horizontal due to the assumption that heat losses to the ambient are negligible. A sharp temperature rise of 50 K characterizes the adiabatic part. In the upper part of the reactor, the cooling effect of the helical coil on the fixed bed is significant in the direct surroundings of the helical coil. Especially at the reactor outlet, the fixed bed is significantly cooled through the cold biogas flowing through the helical coil in a countercurrent stream configuration. Furthermore, it is evident that the cooling effect of the helical coil hardly influences the reactor core.

4.2 Validation with Pilot Plant Operating Data

To validate the shift reactor model, a comparison of 25 experimental steady-state operating points with simulated results is shown in Fig. 7. The temperature measurements agree well with the simulated results, especially for the thermocouples in the fixed bed at z/L = 0.4 and z/L = 0.8 with a maximum deviation of 11 °C. The measured temperature in the HDS reactor indicates the

preheated biogas temperature. This measured biogas preheating temperature corresponds to the simulated temperatures for most operating points.

However, there are five operating points (circled in Fig. 7) at which significantly lower temperatures were measured compared to the simulation. The reason for this could not be fully clarified, but it was possible to determine from the measurement log that these measurement points (load variation) were run after a malfunction in the biogas plant. Due to this malfunction, the load had to be significantly reduced, and the reformer temperature was increased before the load variation measurements. This may have resulted in the temperature measurements not yet being in a steady state. Adjusting the overall heat transfer coefficient for partload operating points may also be necessary.

ded from https://onlinelibrary.wiley.com/doi/10.1002/cite.12007 by Rwth Aachen University

Zentraler Rechnungseingang, Wiley Online Library on [12/06/2025]. See the Term

of use; OA articles are governed by the applicable Creative Commons

The dry molar fractions $y_{\rm CO}$ at the reactor outlet are consistently lower in the simulation compared to the measurements, with a deviation of \sim 0.5 %. This deviation can be due to both experimental errors and simulative assumptions. The equipment for the gas composition measurement was not accurately calibrated, as the data evaluation shows that the mass balance was not satisfied. Additionally, the kinetics of the used commercial catalyst is not known and,

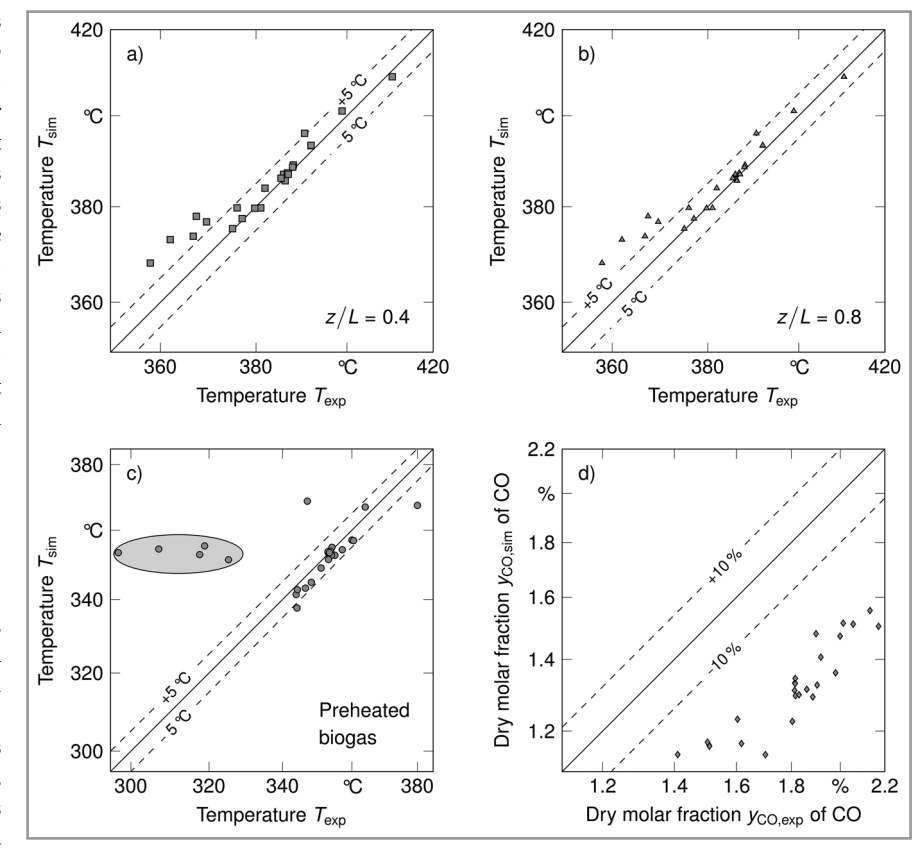


Figure 7. Comparison of experimental and simulated steady-state operating points of temperatures at different positions *z/L* in the shift reactor, biogas preheating temperatures, and outlet gas composition.

15222640, 0, Downloaded from https://onlinelibrary.wiley.com/doi/10.1002/cite.12007 by Rwth Aachen University

eingang, Wiley Online Library on [12/06/2025]. See the Terms

nditions) on Wiley Online Library for rules of use; OA articles are

governed by the applicable Creative Commons

Research Article

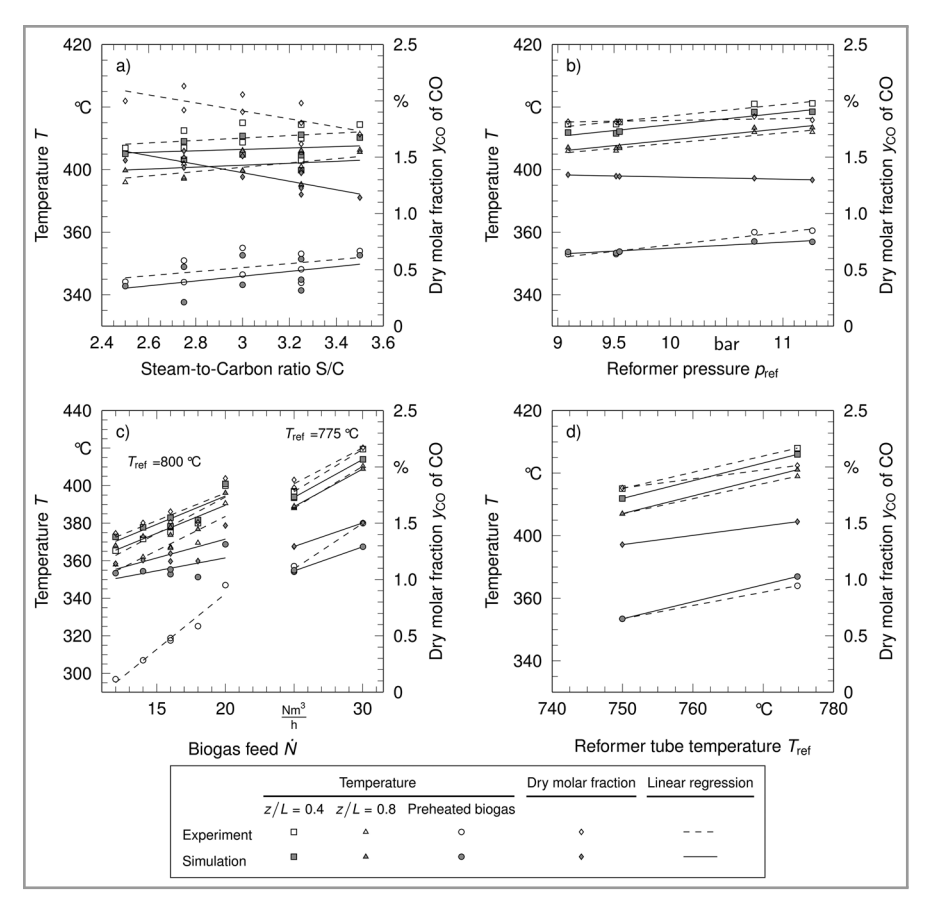


Figure 8. Experimental and simulated steady-state operating points over the varied variables.

therefore, a literature kinetics with identical active components and a similar operating temperature is utilized for simulation. However, the kinetics was measured at atmospheric pressures, not at operating pressures of around 10 bar.

Fig. 8 depicts the operating points from Fig. 7 plotted against the parameter that was varied by step tests on the steam-to-carbon ratio S/C, the reformer pressure p_{ref} , the biogas feed \dot{N} , and the reformer tube temperature $T_{\rm ref}$. Since certain operating points were run multiple times during the measurement campaign, multiple measured temperatures and molar fractions may exist for a single parameter. These measurements cannot be averaged because, contrary to a laboratory setup, step tests on a single variable can never be repeated on a pilot plant. Although every set point of the pilot plant was set to the same value as a previous measurement series, the plant pressure, biogas quality, and environmental influences may have changed. The comparison of the linear trends in Fig. 8 of the measured values with the simulated results indicates good agreement for all parameter variations. Even the simulated molar fraction of CO exhibits a similar trend to the measured CO molar fraction, but with an offset.

The dynamic behavior of the model was validated using experimental data from two exemplary dynamic step tests. As depicted in Fig. 9, a dynamic response of the shift reactor was triggered by a step on the reformer tube temperature. Subsequently, the furnace control system adjusted the burner duty to bring the reformer tube temperature to its new set point. As the shift inlet temperature is not controlled, this step in the reformer tube temperature triggered a change in the shift inlet temperature at z/L = 0.

To replicate this dynamic response, the inlet temperature of the model is set to the measured temperature at the shift reactor inlet via a linear ramp. Additionally, the inlet gas composition of the model is adjusted to approximate measurements of the gas composition at the shift reactor inlet

As illustrated in Fig. 9, the model reproduces the measured dynamic response of the two thermocouples at z/L = 0.4 and z/L = 0.8 in the fixed bed and the biogas preheating temperature accurately, with a maximum deviation of 7 °C. The deviation in the preheated biogas temperature at the new operating point after the

step in the reformer tube temperature might be because this temperature is measured at the HDS reactor and not directly at the shift reactor. The duration of the response following the step change in the reformer tube temperature is also captured reasonably well. Unfortunately, temperature measurements for the outlet temperature at z/L=1 of the shift reactor are not applicable for validation since the reactor flange and subsequent piping are not insulated.

Fig. 10 illustrates the dynamic response of the measured shift reactor temperatures for a step test with a load change from 30 to 25 $\rm Nm^3h^{-1}$. To replicate this response, the biogas feed, the inlet temperature, and the inlet gas composition of the shift reactor are linearly ramped in the model. The model captures the dynamic response reasonably well. However, a considerable deviation of ~ 14 °C in the temperature of the preheated biogas can be noticed at the beginning.

5 Conclusion and Outlook

The production of hydrogen from biogas is a novel utilization route of biogas, which could quickly gain commercial maturity by adopting the well-known natural gas steam

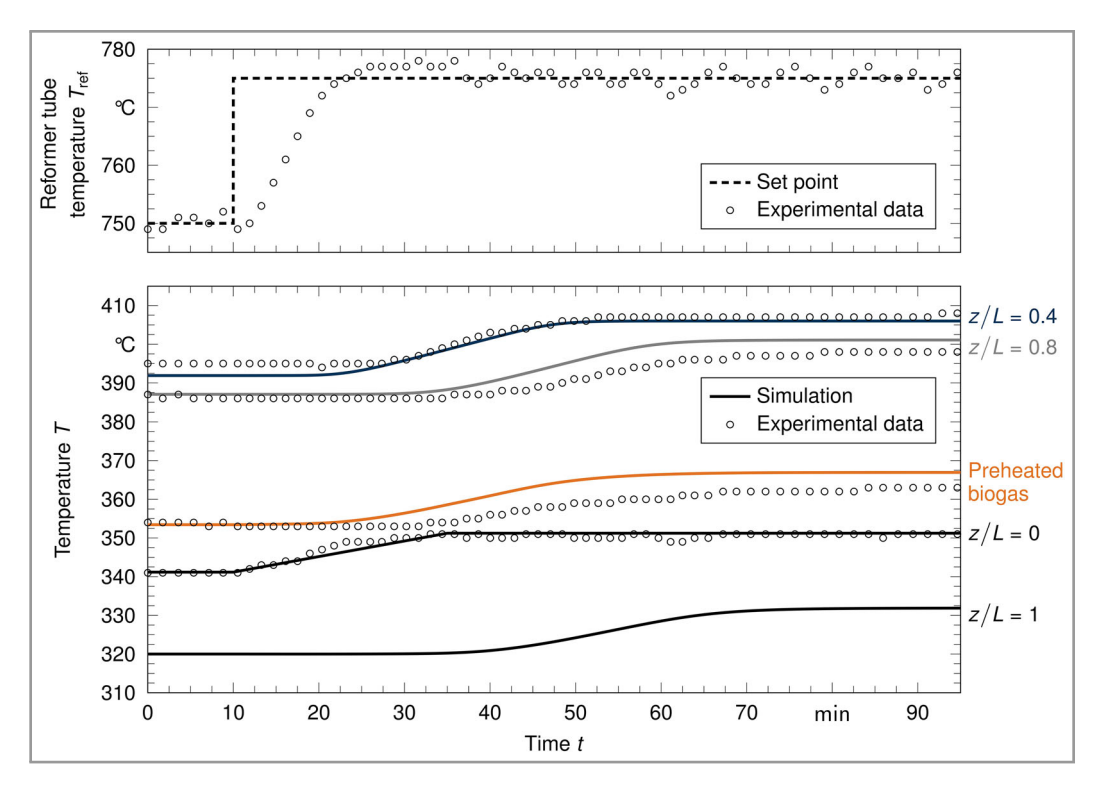


Figure 9. Dynamic behavior of temperatures at different positions *z/L* in the fixed bed and biogas preheating temperatures of the shift reactor during step in reformer tube temperature, with respective model results.

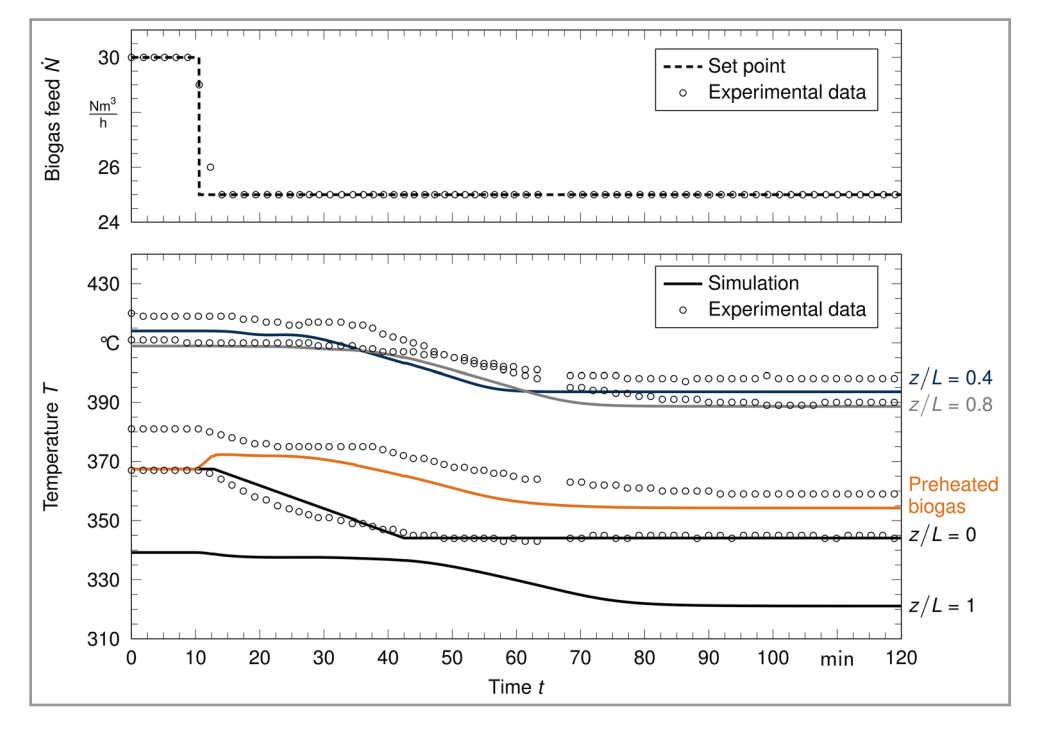


Figure 10. Dynamic behavior of temperatures at different positions *z/L* in the fixed bed and biogas preheating temperatures of the shift reactor during step in biogas feed, with respective model results.

ded from https://onlinelibrary.wiley.com/doi/10.1002/cite.12007 by Rwth Aachen Univ

ingang, Wiley Online Library on [12/06/2025]. See the Term

ons) on Wiley Online Library for rules of use; OA articles are governed by the applicable Creative Commons License

.com/doi/10.1002/cite.12007 by Rwth Aachen University

Rechnungseingang, Wiley Online Library on [12/06/2025]. See the Terms

governed by the applicable Creative Commons License

To understand the working principle of this integrated shift reactor in detail, a 2D, pseudo-homogeneous reactor model was developed and validated with steady-state and dynamic operating data from a pilot steam reforming biogas plant in Krefeld. The model predicts the steady-state operating points and the dynamic response of step tests reasonably well.

Ultimately, the knowledge gained from the detailed shift reactor model will be used to develop a dynamic model of the entire pilot plant. This dynamic model should be capable of predicting the effects of load changes or variations in biogas quality, as well as start-up and shut-down procedures.

Supporting Information

Supporting information for this article can be found under DOI: https://doi.org/10.1002/cite.12007.

Acknowledgements

The authors gratefully acknowledge the financial support of the joint projects BioH2Ref (03EI5440A-C) and BioH2Log (03EI5452B) by the Federal Ministry for Economic Affairs and Climate Action (BMWK) and the project supervision by the project management organization Projektträger Jülich (PtJ).

Open access funding enabled and organized by Projekt DEAL.

Symbols used

$A_{ m 1D}$	$[m^2]$	cross-section of the 1D
		segment
$A_{\rm c}$	$[m^2]$	cross-section of the helical coil
$A_{ m w}$	$[m^2]$	heat transfer area of the helical
		coil
с	$[J kg^{-1}K^{-1}]$	specific heat capacity
$E_{ m A}$	$[kJ \text{ mol}^{-1}]$	activation energy
$F_{ m k}$	[-]	adjustment factor overall heat
		transfer coefficient
F_{λ}	[-]	adjustment factor radial heat
		conductivity
F_{D}	[-]	pressure scale-up factor
r		•

$\Delta ar{H}_R$	$[J \; mol^{-1}]$	molar reaction enthalpy
K	[-]	equilibrium constant
k	$[W m^{-2}K^{-1}]$	overall heat transfer coefficient
LL	[m]	reactor segment length
$L_{\rm c}$	[m]	length of the helical coil
\dot{M}	$[kg s^{-1}]$	mass flow rate
$ar{M}_i$	[kg kmol ⁻¹]	molar mass of component i
\dot{N}	$[\mathrm{Nm}^3\mathrm{h}^{-1}]$	molar flow rate
h	$[J kg^{-1}]$	specific enthalpy
p	[Pa]	pressure
p_i	[kPa]	partial pressure of
		component i
ġ	$[W m^{-2}]$	heat flux
ġ Ā	$[kJ \text{ mol}^{-1}K^{-1}]$	molar universal gas constant
$R_{\rm i}$	[m]	inner radius of the domain
$R_{\rm o}$	[m]	outer radius of the domain
rr	[m]	radial domain
$r_{\rm reac}$	[kmol kg _{cat} ⁻¹ s ⁻¹]	molar reaction rate
T	[°C], [K]	temperature
t	[s]	time domain
ũ	$[J m^{-3}]$	volume-specific internal
		energy
ν	$[m s^{-1}]$	superficial velocity
w_i	[-]	mass fraction of component i
y_i	[-]	molar fraction of component i
ZZ	[-]	auxiliary quantity (equilibrium
		constant)
z	[m]	axial domain
z'	[m]	axial domain of the helical coil

Greek symbols

ε	[-]	porosity
$\lambda_{ m e}$	$[W m^{-1}K^{-1}]$	radial effective heat
		conductivity
ν_i	[-]	stoichiometric number of
		component i
ρ	$[kg m^{-3}]$	density
ρ_i	$[kg m^{-3}]$	partial density of component i

Sub-/superscripts

0	inlet condition
b	biogas
cat	catalyst
exp	experimental data
ref	reformer
sim	simulation

Abbreviations

1D	one-dimensional
2D	two-dimensional

EEG Renewable Energy Sources Act

HDS hydrodesulfurization

HT high-temperature

LT low-temperature

PSA pressure swing adsorption

S/C steam-to-carbon ratio

WGS water-gas shift

References

- E. Weidner, W. Urban, K. Girod, H. Lohmann, Technologien und Kosten der Biogasaufbereitung und Einspeisung in das Erdgasnetz. Ergebnisse der Markterhebung 2007-2008, Fraunhofer UMSICHT, Oberhausen 2009.
- [2] P. Adler, E. Billig, A. Brosowski, J. Daniel-Gromke, I. Falke, E. Fischer, J. Grope, U. Holzhammer, J. Postel, J. Schnutenhaus, et al., *Leitfaden Biogasaufbereitung und -einspeisung*, 5th ed., FNR, Gülzow-Prüzen 2014.
- [3] M. Persson, O. Jönsson, A. Wellinger, Biogas Upgrading to Vehicle Fuel Standards and Grid Injection, IEA Bioenergy, Malmö 2006
- [4] Fachverband Biogas, Branchenzahlen 2022 und Prognose der Branchenentwicklung 2023, Fachverband Biogas, Freising 2023.
- [5] DESTATIS, Stromerzeugung 2023: 56 % aus erneuerbaren Energieträgern, Pressemitteilung Nr. 087, DESTATIS, Wiesbaden 2024.
- [6] J. Daniel-Gromke, N. Rensberg, V. Denysenko, T. Barchmann, K. Oehmichen, M. Beil, W. Beyrich, B. Krautkremer, M. Trommler, J. Vollprecht, et al., Optionen für Biogas-Bestandsanlagen bis 2030 aus ökonomischer und energiewirtschaftlicher Sicht, Umweltbundesamt, Dessau-Roßlau 2020.
- [7] P. Matschoss, B. Wern, F. Baur, Die Bioenergie in der Energiewende und die "Post-EEG-Frage" – Eine Synopse von Post-EEG-Studien, IZES, Saarbrücken 2024.
- [8] M. Paterson, M. Dotzauer, P. Matschoss, N. Rensberg, B. Wern, Auswertung von Post-EEG-Projekten – Schlussfolgerungen für die Biogas-Praxis, KTBL, Darmstadt 2024.
- [9] N. Grösch, C. Trox, A. Saidi, W. Zörner, V. Grüner, D. Baumkötter, E. Brügging, C. Wetter, M. Glötzl, U. Kilburg, et al., Biogas nach dem EEG (wie) kann's weitergehen?, 4th ed., C.A.R.M.E.N. e.V., Straubing 2024.
- [10] IEA, The Future of Hydrogen Seizing Today's Opportunities, IEA, Paris 2019.
- [11] IEA, Global Hydrogen Review 2024, IEA, Paris 2024.
- [12] A. Gradel, G. Pauletto, U. Mach, T. Birth-Reichert, J. Hanke, gwf Gas + Energie 2023, 164 (10), 54–59.
- [13] K. Aasberg-Petersen, I. Dybkjær, C. V. Ovesen, N. C. Schjødt,
 J. Sehested, S. G. Thomsen, J. Nat. Gas Sci. Eng. 2011, 3 (2),
 423–459. DOI: https://doi.org/10.1016/j.jngse.2011.03.004
- [14] B. Smith R J, M. Loganathan, M. S. Shantha, Int. J. Chem. React. Eng. 2010, 8 (1). DOI: https://doi.org/10.2202/1542-6580. 2238

- [15] H. A. J. Van Dijk, D. Cohen, A. A. Hakeem, M. Makkee, K. Damen, *Int. J. Greenhouse Gas Control* 2014, 29, 82–91. DOI: https://doi.org/10.1016/j.ijggc.2014.07.005
- T. A. Adams II, P. I. Barton, Int. J. Hydrogen Energy 2009, 34 (21), 8877–8891. DOI: https://doi.org/10.1016/j.ijhydene.2009.08.
 045
- [17] S. R. Janbarari, A. Taheri Najafabadi, Int. J. Hydrogen Energy 2023, 48 (64), 25158–25170. DOI: https://doi.org/10.1016/j. iihvdene.2022.12.355
- [18] O. L. Ding, S. H. Chan, Int. J. Hydrogen Energy 2008, 33 (16), 4325–4336. DOI: https://doi.org/10.1016/j.ijhydene.2008.05.087
- [19] P. Giunta, N. Amadeo, M. Laborde, J. Power Sources 2006, 156 (2), 489–496. DOI: https://doi.org/10.1016/j.jpowsour.2005. 04.036
- [20] P. Kumar, E. Akpan, H. Ibrahim, A. Aboudheir, R. Idem, *Ind. Eng. Chem. Res.* 2008, 47 (12), 4086–4097. DOI: https://doi.org/10.1021/ie071547q
- [21] J. A. Francesconi, M. C. Mussati, P. A. Aguirre, J. Power Sources 2007, 173 (1), 467–477. DOI: https://doi.org/10.1016/j.jpowsour. 2007.04.048
- [22] N. H. Bell, T. F. Edgar, J. Process Control 1991, 1 (1), 22–31.
 DOI: https://doi.org/10.1016/0959-1524(91)87004-H
- [23] N. H. Bell, T. F. Edgar, J. Process Control 1991, 1 (2), 59–67. DOI: https://doi.org/10.1016/0959-1524(91)80002-2
- [24] G. T. Wright, T. F. Edgar, Comput. Chem. Eng. 1994, 18 (2), 83– 102. DOI: https://doi.org/10.1016/0098-1354(94)80130-4
- [25] V. P. Paixão, L. F. M. Franco, J. V. H. D'Angelo, *Ind. Eng. Chem. Res.* 2020, 59 (49), 21429–21438. DOI: https://doi.org/10.1021/acs.iecr.0c03262
- [26] S. Z. Saw, J. Nandong, IOP Conf. Ser.: Mater. Sci. Eng. 2016, 121, 012022. DOI: https://doi.org/10.1088/1757-899X/121/1/012022
- [27] F. Rosner, A. Rao, S. Samuelsen, Appl. Therm. Eng. 2020, 173, 115033. DOI: https://doi.org/10.1016/j.applthermaleng.2020. 115033
- [28] S. Ergun, Chem. Eng. Prog. 1952, 48 (2), 89-94.
- [29] VDI-Wärmeatlas (Eds: P. Stephan, S. Kabelac, M. Kind, D. Mewes, K. Schaber, T. Wetzel), 12th ed., Springer, Berlin 2019.
- [30] P. Zehner, E. U. Schlünder, Chem. Ing. Tech. 1970, 42 (14), 933–941. DOI: https://doi.org/10.1002/cite.330421408
- [31] V. Specchia, G. Baldi, S. Sicardi, Chem. Eng. Commun. 1980, 4 (1-3), 361-380. DOI: https://doi.org/10.1080/ 00986448008935916
- [32] V. Gnielinski, Forsch. Ingenieurwes. 1975, 41 (5), 145–153. DOI: https://doi.org/10.1007/BF02560793
- [33] V. Gnielinski, in Proceedings of the International Heat Transfer Conference 8, Begellhouse, San Francisco 1986.
- [34] S. S. Hla, D. Park, G. J. Duffy, J. H. Edwards, D. G. Roberts, A. Ilyushechkin, L. D. Morpeth, T. Nguyen, *Chem. Eng. J.* 2009, 146 (1), 148–154. DOI: https://doi.org/10.1016/j.cej.2008.09.023
- [35] M. V. Twigg, Catalyst Handbook, 2nd ed., Manson Publishing, London 1989.
- [36] K. Atwood, M. R. Arnold, E. G. Appel, Ind. Eng. Chem. 1950, 42 (8), 1600–1602. DOI: https://doi.org/10.1021/ie50488a038
- [37] C. P. P. Singh, D. N. Saraf, Ind. Eng. Chem. Process Des. Dev. 1977, 16 (3), 313–319. DOI: https://doi.org/10.1021/i260063a012